Surface & Coatings Technology 446 (2022) 128806

Contents lists available at ScienceDirect

Surface & Coatings Technology

journal homepage: www.elsevier.com/locate/surfcoat

Revisiting the origins of super-hardness in TiB_{2+z} thin films – Impact of growth conditions and anisotropy

C. Fuger [a,*], R. Hahn [a], A. Hirle [a], P. Kutrowatz [a], M. Weiss [b], A. Limbeck [b], O. Hunold [c], P. Polcik [d], H. Riedl [a,e]

[a] Christian Doppler Laboratory for Surface Engineering of High-performance Components, TU Wien, A-1060 Vienna, Austria
[b] Institute of Chemical Technologies and Analytics, TU Wien, A-1060 Vienna, Austria
[c] Oerlikon Balzers, Oerlikon Surface Solutions AG, 9496 Balzers, Liechtenstein
[d] Plansee Composite Materials GmbH, D-86983 Lechbruck am See, Germany
[e] Institute of Materials Science and Technology, TU Wien, A-1060 Wien, Austria

ARTICLE INFO

Keywords:
TiB_2
Stoichiometry
Anisotropy
Super-hardness
Fracture toughness

ABSTRACT

Hexagonal transition metal diborides embody promising material systems for the purpose of protective thin films. Here, we focus on DC magnetron sputtered TiB_{2+z} coating materials, comprehensively revisiting the impact of the stoichiometry on the structure-mechanical properties, from nearly stoichiometric $TiB_{2.07}$ (B: 67 at. %) up to super-stoichiometric $TiB_{4.42}$ (B: 82 at. %). The structural analysis confirmed the apparent correlation between the deposition pressure and the preferred {0001} orientation, which is essential to gain super-hardness (>40 GPa). In contrast, the hardness decreases for >10 GPa for $10\bar{1}1$ and 1000 oriented thin films, underlining the pronounced anisotropy of TiB_{2+z}. The broad stoichiometry variation revealed no predominant hardness effect based on a B-rich tissue phase. The excess B contributes to a decreasing column size correlating with a decreasing hardness of ≈ 7 GPa (B/Ti ratios >2.5) due to column boundary sliding events. Micro-cantilever bending experiments proved a declining fracture toughness from 3.02 ± 0.13 MPa$\sqrt{m}$ for $TiB_{2.43}$ to 2.51 ± 0.14 MPa$\sqrt{m}$ for $TiB_{4.42}$ to be column size dependent.

1. Introduction

TiB_2 thin film materials are an extensively researched subject, due to their highly promising material characteristics. In the early stages non reactively and reactively sputtered TiB_2 was investigated for its abilities as a boron diffusion source, or as diffusion barrier between Si and Al as well as Au and Au/Ge/Ni [1–4]. Subsequently, its outstanding physical and mechanical properties, including low density of 4.5 g/cm^3, high melting temperature of 3225 °C, low electrical resistivity of 7μΩcm, and especially very high hardness (>40 GPa) made it also attractive for industrial applications [5–7]. Further interesting properties could be listed here, but are already carefully adduced within the introduction part of the referenced works. One major drawback of TiB_2 is the low oxidation resistance of ≈400 °C, which is influenced by varying B content [8,9]. Nevertheless, Glechner et al. demonstrated a decisive improvement of the oxidation behavior by silicon alloying, accompanied by a pronounced reduction in film hardness of >10 GPa [10]. The mechanical properties of TiB_2 vary a lot in literature (from 20 to 50 GPa), mainly due to the use of different deposition techniques (balanced/unbalanced DCMS, ICP assisted PVD, HiPIMS, etc.), and growth parameters [6,7,11–14]. Hence, strongly influencing the characteristics, morphology and stoichiometry of the synthesized thin films, causing the perspicuous deviation in mechanical properties. In literature, a B-rich tissue phase forming at super-stoichiometric TiB_{2+z} compositions is described as an important factor [11]. It is supposed to prevent grain boundary sliding and therefore cause enhanced hardness [11]. Such a tissue phase was also observed for ZrB_{2+z} [15] and sub-stoichiometric NbB_{2-z} [16]. Nevertheless, sub-stoichiometric TiB_{2-z} exhibits comparably high mechanical properties, but synthesized in [13] by HiPIMS, may also superimpose other effects owing to enhanced growth conditions through ionized species. As already addressed by H. Holleck in 1986, the hardness of TiB_2 and TiC differ by ≈30 % depending on the crystal orientation [5]. The same effect of an anisotropic hardness was already observed for physical vapor deposited, hexagonal (SG191, P6mmm) WB_{2-z} coatings [17]. However, only minor attention has been given to this effect in literature so far, as in [11] Mayrhofer et al.

* Corresponding author at: Christian Doppler Laboratory for Surface Engineering of High-performance Components, TU Wien, A-1060 Vienna, Austria.
E-mail address: christoph.fuger@tuwien.ac.at (C. Fuger).

https://doi.org/10.1016/j.surfcoat.2022.128806
Received 13 April 2022; Received in revised form 11 August 2022; Accepted 15 August 2022
Available online 17 August 2022

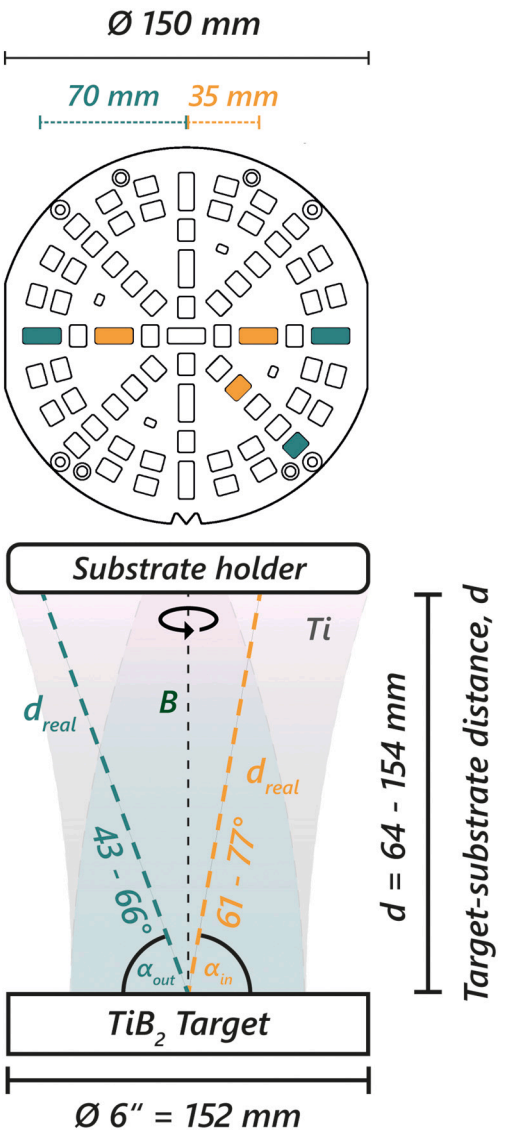

Fig. 1. Illustration of the used substrate and deposition arrangement for all the synthesized TiB_{2+z} films.

predominately contributed the high hardness to the formed tissue phase in $TiB_{2.4}$. The mechanisms behind the pronounced deviation from stoichiometric TiB_2 are delineated in detail by Neidhardt et al. [18]. Based on pressure, distance and angular variations in DCMS deposition experiments (accompanied by theoretical simulations), they found that sputtered B atoms are preferentially emitted along the target normal, while Ti atoms follow a shallower distribution. A pathway for controlling the B/Ti ratio of TiB_x coatings by unbalanced magnetron sputtering is given by Petrov et al. [19]. Both studies offer a reliable basis to consciously adjust the B-content, causing a change in mechanical properties. Beyond residual stresses, hardness and Young's modulus, only few studies investigated the influence of B on ductility measures, such as fracture toughness of $TiB_{2\pm z}$ [13,20].

Here, we first time offer intrinsic K_{IC} values of super-stoichiometric DCMS TiB_{2+z} thin films, by micro cantilever bending experiments. To get a broad variation in B we adapted the findings from Neidhardt et al. [18] to our deposition pathway and give an interpretation of varying mechanical properties and their underlying effects. Moreover, the importance of the predominant film orientation and how it can be altered, is highlighted.

2. Methods

2.1. Thin film deposition

An in-house developed DC magnetron sputter deposition system [21] with a central arranged cathode was used for the synthesis of the TiB_{2+z} coatings. The ultra-high vacuum coating facility was equipped with a 6-inch powder metallurgical produced TiB_2/C 99/1 wt% target (Plansee Composite Materials GmbH, purity >99.6 %). The minor amount of C contributes to an improved conductivity of the target material and results in a C content of below 1.5 at.% within the coatings, comparable to other residuals like N, O and Ar. Prior to the depositions, silicon (20 × 7 × 0.38 mm^3), polished single crystalline sapphire (10 × 10 × 0.5 mm^3, $1\bar{1}02$ oriented), and polished austenitic steel (20 × 7 × 1 mm^3) substrates were ultrasonically pre-cleaned in acetone and ethanol for 5 min each. Subsequently, they were mounted on a rotating substrate holder, and heated up in the chamber (base pressure below $4{\cdot}10^{-4}$ Pa) to the deposition temperature, T_{dep}, of 700 °C (corresponding to 500 ± 15 °C on the substrate surface) for 30 min. In accordance to Neidhardt et al. [18] (angular distribution of sputtered B/Ti species) the substrates where placed on the very inner and outer radius of the substrate holder as illustrated in Fig. 1.

Furthermore, the substrates were etched in argon atmosphere (p_{etch} = 5 Pa) for 15 min applying a DC substrate potential of −1000 V. The last 3 min of the etching procedure were used for simultaneously pre-sputtering also the target behind a shutter. This procedure was carried out, to get rid of oxygen on the target surface as well as to ensure a stable deposition plasma. The depositions were also done in pure argon atmosphere varying the pressure (p_{dep} = 0.4, 0.6, 0.8, 1.2, 1.6, 2.0 Pa) at constant target to substrate distance of d = 104 mm. The variation of the target to substrate distance (d = 64, 84, 104, 114, 124, 134, 154 mm) was performed at constant deposition pressure of 0.4 Pa. As indicated in Fig. 1, the variation in distance also leads to a variation in the so-called deposition angle α_{out} = 43–66° for substrates placed on the outer radius, and α_{in} = 61–77° for those placed on the inner radius. The TiB_2/C target was powered by a Solvix HIP3 generator used in DC mode with a maximum target current, I_{target}, of 4 A leading to a 9 W/cm^2 power density during deposition. The deposition time was set between 45 and 60 min using a rotating substrate holder with rotation speed of 45°/s. The film growth was also supported by applying a DC bias potential of -50 V.

2.2. Chemical and structural analysis

The elemental composition of the TiB_{2+z} thin films on sapphire (Sa) substrates were analyzed by liquid inductively coupled plasma optical emission spectroscopy (LICP-OES). LICP-OES measurements were carried out on an iCAP 6500 RAD (Thermo Fisher Scientific, USA), with an ASX-520 autosampler (CETAC Technologies, USA) using an HF resistant sample introduction kit, consisting of a Miramist nebulizer (Burger Research, USA), a PTFE spray chamber and a ceramic injector tube. For the chemical analysis the TiB_{2+z} samples were broken into pieces of about 3 × 3 mm^2 and the thin film with the substrate was dissolved with

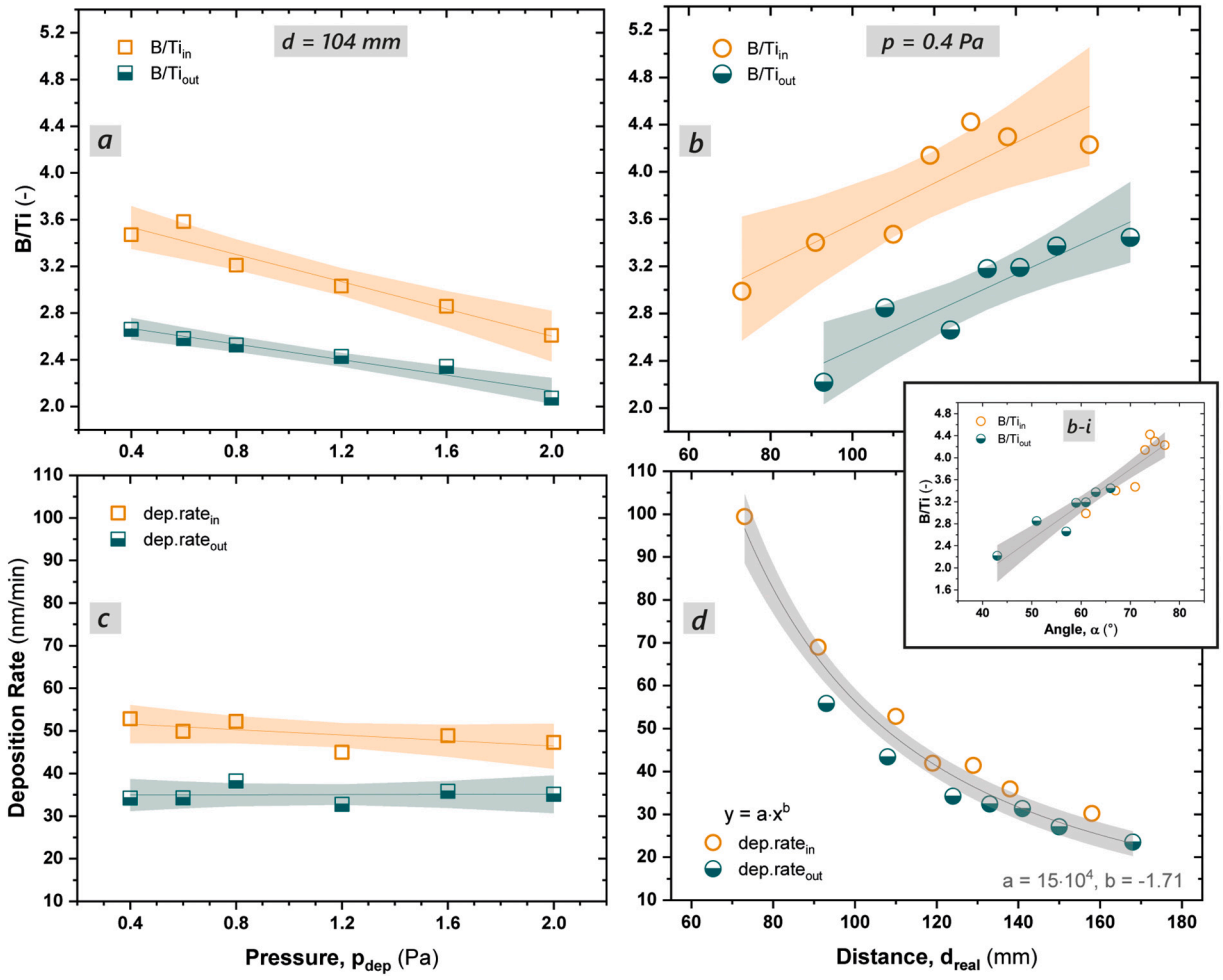

Fig. 2. Influence of deposition pressure, p_{dep}, and real target-substrate distance d_{real} on the B/Ti ratio (a, b) and deposition rate (c, d), respectively. Moreover, the inset b-i shows the influence of the deposition angle α on the B/Ti ratio. Orange open symbols indicate the substrates placed on the inner radius ($r = 35$ mm) of the substrate holder, while green half-filled symbols represent the samples placed on the outer radius ($r = 70$ mm). The synthesized films deriving from p_{dep} and d_{real} variation are indicated by squares and circles. The data in a-c has been fitted by linear functions and the 95 % confidence band [26] is depicted by the orange, green and grey shaded areas. The mathematical function and coefficients used in section d are provided.

a mixture of 1 mL HNO_3 and 0.25 mL HF. After a reaction time of 15 min at a temperature of 60 °C, the thin film including the substrate was completely dissolved. Derived sample digests were diluted to a final volume of 20 mL with a mixture of 3 % HNO_3 and 0.3 % HF. Quantification was done via external calibration using matrix adjusted standards. The relative uncertainty of the chemical compositions deduced from the LICP-OES technique, considering both systematic and statistical uncertainties is around 2 % [22].

A Philips XPERT diffractometer in Bragg-Brentano configuration was used for detailed structural analysis. The diffractometer was equipped with a Cu-K_α ($\lambda = 1.54187$ Å) radiation source. The software 'HighScore' was used for evaluating the intensities of the diffraction peaks to calculate the texture coefficients and {0001} fractions of the TiB_{2+z} coatings (see Appendix A for details to the calculations). Hence, the background of the XRD pattern was determined automatically after the method of Sonneveld & Visser [23]. The "Pearson 7" profile function with asymmetry type "Split Width and Shape" was used to reach satisfactorily peak fits. No asymmetry function was applied to evaluate the FWHM of the selected thin films. Moreover, Scherrer's formula was used to determine the crystallite size of the columnar structured thin films:

$$d = \frac{K \cdot \lambda}{FWHM \cdot cos(\theta)} \quad (1)$$

Utilizing a crystal shape factor $K = 0.9$ and $\lambda = 1.540598$ Å (Cu-$K_{\alpha 1}$). The values of d were calculated manually using an LaB_6 standard to determine the instrumental broadening ($B_{std} \approx 0.09°2\theta$) which was subtracted from the experimentally observed broadening.

TEM investigations of the microstructure have been performed by a FEI TECNAI F20, equipped with a field emission gun and operated at an accelerating voltage of 200 kV. The TEM top view samples were prepared using the standard FIB lift-out method on a selected surface-near region.

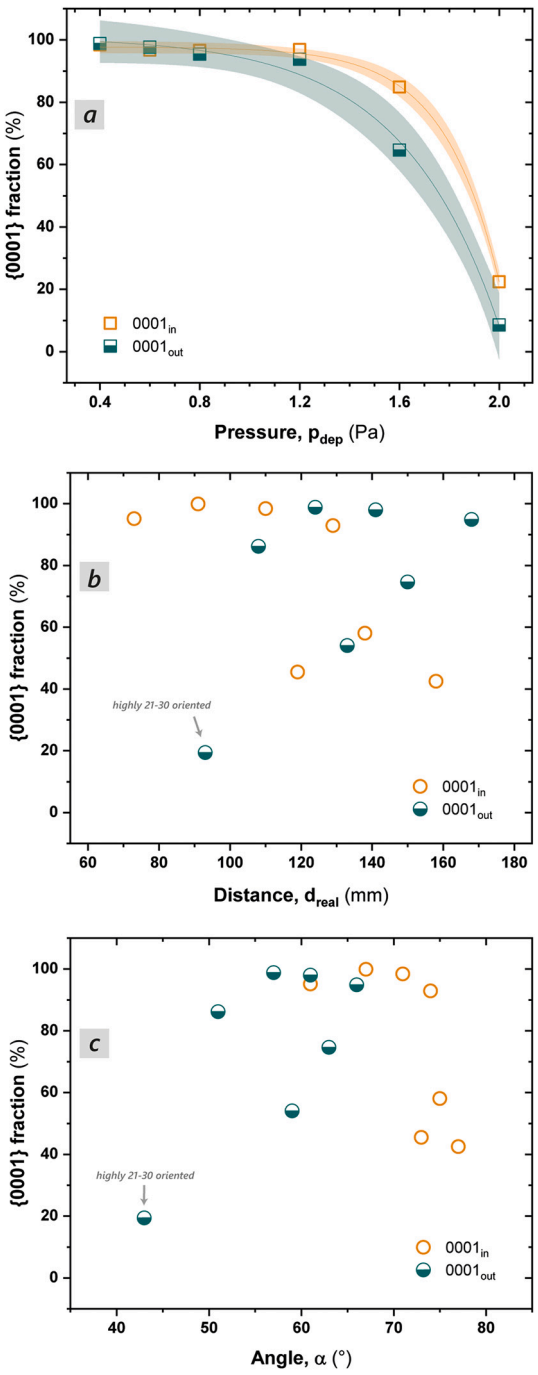

Fig. 3. The {0001} orientation fraction was determined by evaluating the XRD pattern of all deposited TiB_{2+z} films and is depicted as a function of the deposition pressure p_{dep} (a) and real sputter distance d_{real} (b) and deposition angle α (c). Orange open and green half-filled symbols indicate substrates placed on inner and outer radii of the circular substrate holder, respectively. In (a) the best fitting mathematical function (exponential decay) and the 95 % confidence band [26] is illustrated (orange and green shaded areas).

2.3. Nanoindentation

Hardness, H, and Young's modulus, E, of the coating was analyzed by an Ultra Micro Indentation System (UMIS). The applied three-sided Berkovich diamond tip (E = 1050 GPa and Poisson's ratio $\nu = 0.07$) was calibrated with a fused silica reference sample (E = 72.5 GPa, H = 10 GPa). An area function was determined to ensure appropriate results by measuring the fused silica sample in various force ranges, obtaining a plastic depth of 70 nm. 35 indentations covering a force range from 5 mN to 30 mN were performed to establish the indentation properties of the TiB_{2+z} film on austenitic steel substrate. The resulted load displacement curves were corrected with instrument compliance, initial penetration and area function. Subsequently, the well-established approach from Oliver and Pharr [24] was used for evaluating H and E* of the TiB_{2+z} film. A Poisson's ratio of $\nu = 0.15$ was adopted to calculate E out of the combined modulus and tip modulus. Furthermore, E was determined by a power law fit of all measured E values as a function of the indentation depth, h.

2.4. Micromechanical testing

In situ micromechanical bending tests of substrate-free coating cantilevers were conducted to obtain the intrinsic fracture toughness of the TiB_{2+z} coatings. The cantilevers were shaped by FIB milling from coatings on austenitic steel substrates. The experiments were performed within an SEM equipped with a FemtoTools NMT-04 in-situ nano-indentation system whose wedge diamond tip was pressed onto the top of the pre-notched cantilever (in the growth direction of the coatings) until fracture. The calculation of the fracture toughness was performed after the linear elastic approach developed by Matoy et al. [25]. For the fracture toughness evaluation, the following equation was used:

$$K_{IC} = \frac{P_{max}L}{BW^{\frac{3}{2}}}\left(1.46 + 24.36\left(\frac{a}{w}\right) - 47.21\left(\frac{a}{w}\right)^2 + 75.18\left(\frac{a}{w}\right)^3\right) \quad (2)$$

with P_{max} being the maximum force during loading, L the cantilever length, B, the width, w the height, and a the initial notch depth. The dimensions of the cantilever were determined using the above-mentioned SEM (Zeiss Sigma 500 VP FEGSEM).

3. Results and discussion

To comprehensively describe the influence of the stoichiometry on structure-mechanical properties, a broad variation in chemical compositions of TiB_{2+z} thin films is required. Therefore, to cover this broad range in stoichiometries, the deposition pressure and target to substrate distance have been varied to influence the B/Ti ratio during DC magnetron sputtering of TiB_2. These deposition related aspects are summarized in Fig. 2, where a variation from $TiB_{2.07}$ (Ti: 33 at. %, B: 67 at. %) up to $TiB_{4.42}$ (Ti: 18 at. %, B: 82 at. %) is achieved. Based on the findings from Neidhardt et al. [18] – experimentally investigating the distribution of B and Ti species in the sputter plasma, as well as theoretically by TRIM and TRIDYM simulations – the surplus of B on inner radii compared to outer radii placed samples is obvious (see Fig. 2a and b, open and half-filled symbols, respectively). The emission of B atoms is unambiguously more pronounced along the vicinity of the target

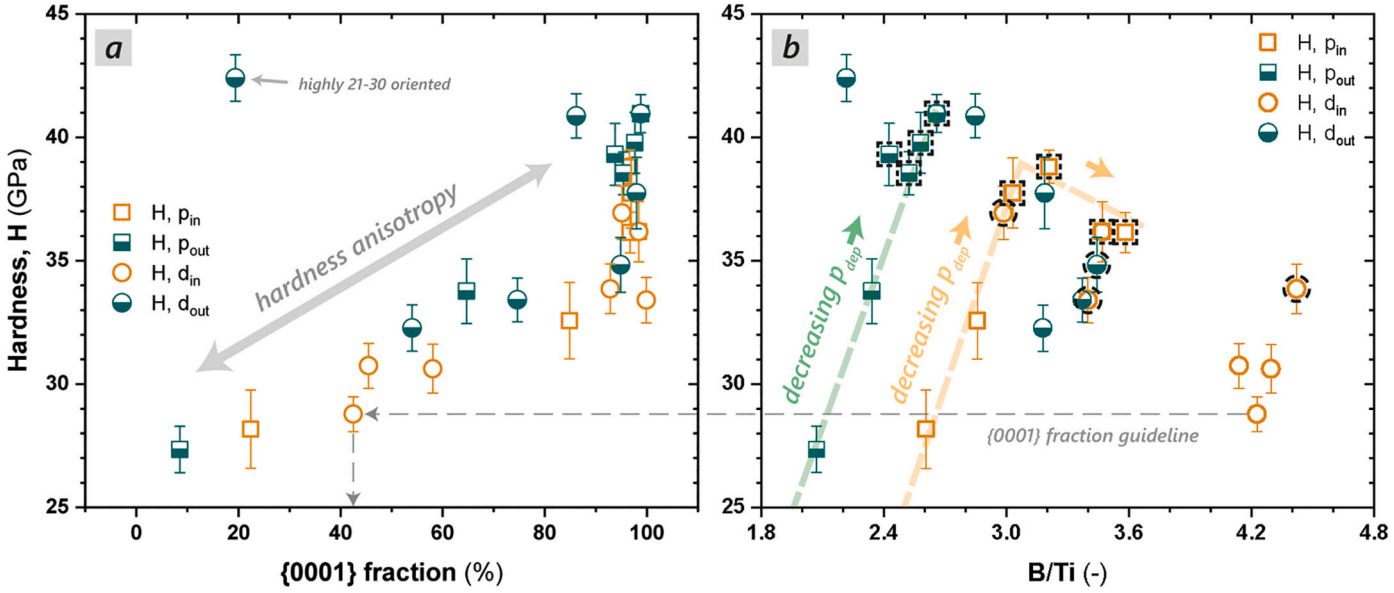

Fig. 4. Hardness H of all deposited TiB_{2+z} thin films, determined by nanoindentation, is illustrated as a function of {0001} fraction (a) and B/Ti ratio (b). Inner and outer radii placed samples are depicted by open orange and half-filled green symbols. Square and circular data points indicate coatings derived from deposition pressure and distance variation, respectively. The orange and green dashed lines (Fig. 4b) indicate films from inner and outer radii, derived from the deposition pressure variation. Thin films exhibiting a {0001} fraction >90 % are marked with black dashed square and circular frames.

normal, increasing the B content on the inner radii. By increasing the deposition pressure from 0.4 to 2.0 Pa, the B/Ti ratio of inner and outer positions decrease similar (see Fig. 2a). However, the slightly increased slope of the B/Ti ratio on the inner radius (indicated by the linear fit of the open orange squares) suggests a higher collision probability along the target normal due to an increased number of sputtered species. Moreover, the decreasing offset of the B/Ti ratio (see orange and green linear fit in Fig. 2a) between inner and outer positions with increasing deposition pressure, indicates that the B sputter plume is even more pronounced along the vicinity of the target normal at low deposition pressure. Contrary to Fig. 2a, Fig. 2b shows an increasing B content with increasing real sputter distance d_{real} (including deposition angle α according to Fig. 1) for both radii. This is in contrast to the findings from Neidhardt et al. [18], observing a decreasing B/Ti ratio with increasing sputter distance, but investigated the relation at a deposition pressure of 2 Pa (at ≈ 5 W/cm^2) compared to 0.4 Pa (at ≈ 9 W/cm^2) within this study. The already mentioned effect of a more pronounced and further reaching B sputter plume along the target normal at low pressures again explains this behavior. The variation in the substrate positions also leads to a variation in the theoretical target to substrate angle α_{in} and α_{out} (see deposition arrangement in Fig. 1). Linearly increasing B can also be observed for increasing angle α, as illustrated in the inset b-i of Fig. 2b. The film thicknesses of the synthesized coatings are analyzed by SEM and divided by the deposition time to determine the deposition rate. The slightly decreasing deposition rates with increasing pressures for the inner substrate positions and the constant behavior for the outer positions (see Fig. 2c) suggest minor collision-induced effects. The $\approx 1/d^2$ dependency of the deposition rate, indicated by the grey marked fit in Fig. 2d, also underlines a propagation of the sputtered species, which is only minor influenced by collisions as observed in [18].

The structural evolution in relation to the obtained stoichiometries is analyzed by XRD. To highlight the {0001} orientation fraction of the deposited TiB_{2+z} thin films, the intensities of equivalent 0001 peaks (0001, 0002, 0003), in relation to all visible crystallographic relevant (SG191, P6mmm [27]) peaks, are calculated using Formula (A2) (see Appendix A). Formula (A2) does not include the reference intensities I_0 of a randomly oriented powder diffraction pattern leading to unweighted peak intensities. For comparison, the 0001 texture coefficient (TC_{0001}) [28] is calculated using the mathematical approach given by Formula (A1) in the Appendix A section and results are listed in Table A2. The received {0001} fraction is illustrated as a function of increasing p_{dep} (Fig. 3a) and discloses an exponential decrease. Films deposited at a deposition pressure from $p_{dep} = 0.4$ to 1.2 Pa at constant target-substrate distance of d = 104 mm, exhibit almost solely {0001} oriented crystallites. After exceeding $p_{dep} = 1.2$ Pa the dominance of the {0001} orientation decreases exponentially with increasing p_{dep} and the $10\bar{1}1$ orientation gets predominant – next to minor 1000 fractions. Utilizing density functional theory (DFT) calculations Zhang et al. [29] investigated the surface stabilities of MB_2 (M = Ti, Zr, Hf). Considering the chemical potentials μ at the surface slabs of their supercells, they found that $(10\bar{1}1)_{B(M)}$ and $(0001)_B$ surfaces are thermodynamically most preferred, while the pyramidal $(10\bar{1}1)_{B(M)}$ surface exhibits the widest stability range for TiB_2, HfB_2 and ZrB_2. For TiB_2 the study revealed a most stable $(0001)_{B(Ti)}$ surface followed by a broad stability range for the $(10\bar{1}1)_{B(Ti)}$ surface, when moving from B-rich to M-rich environments. Moreover, the thermodynamically preferred surfaces are also associated with relatively low cleavage energy and surface strain. In our study, the dependence of the chemical potential on the preferred orientation seems to be less dominant. In contrast, the energy of the sputtered particles according to the mean free path (MFP) mainly contributes to the transition in orientation. The data points arising from the variation in deposition pressure underline this (following the green and orange dashed lines in Fig. 4b) by exhibiting a change in film orientation at

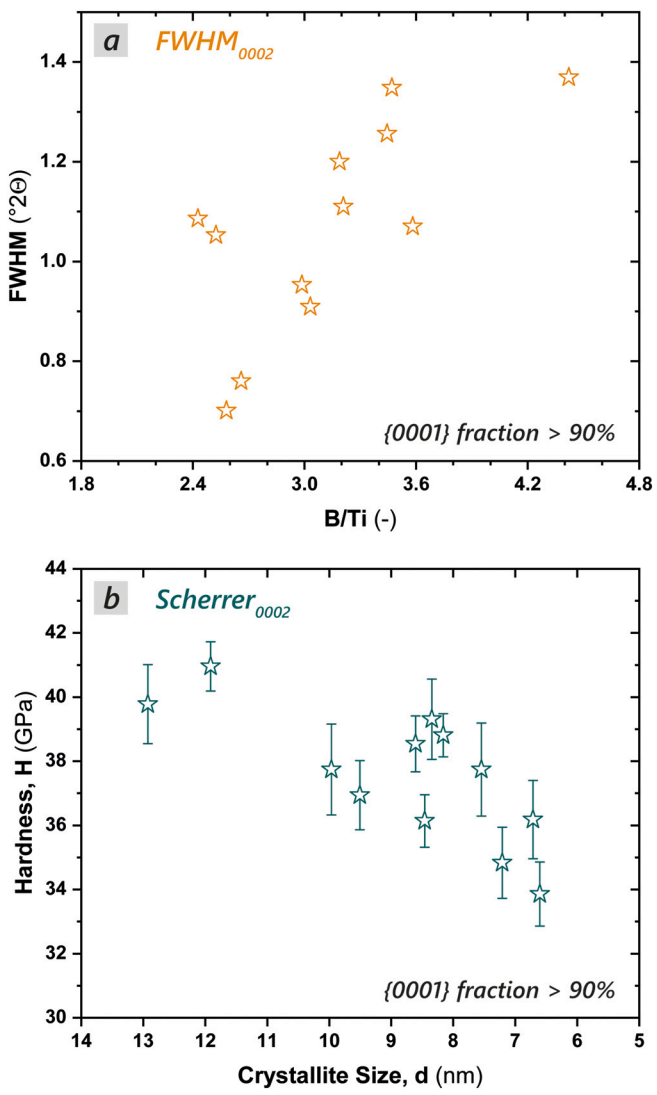

Fig. 5. Evaluated $FWHM_{0002}$ of all deposited thin films with a {0001} fraction >90 % (a). The FWHM of the 0002 diffraction peaks (see Appendix A for XRD data) as a function of the films B/Ti ratio is depicted by yellow stars. In Fig. 5b the hardness values of the consulted coatings as a function of column size d (applying the Scherrer equation to the 0002 peak) are highlighted.

different B/Ti ratios.

In contrast to the variation in deposition pressure p_{dep}, no clear trend in {0001} fraction is visible for the changing real target-substrate distance d_{real} (Fig. 3b). However, a dependence of the target-substrate angle α (Fig. 3c) is perceptible, revealing predominant 0001 oriented films at α = 57° - 71°. Moreover, very close distances and low angles (the arrow indicates the data point in Fig. 3b) support the formation of the $21\bar{3}0$ orientation, which is also already slightly detectable for the closest 0001_{in} data point in Fig. 3b and c (but revealing α > 60°).

As observed for hexagonal (SG191, P6mmm) WB_{2-z} thin films [17], the hardness of TiB_{2+z} as well exhibits a tremendous dependence on the orientation, which was already suggested by Holleck in 1986 [5]. Nevertheless, our study provides now a broad insight with respect to synthesis related stoichiometries as highlighted in Fig. 4. In Fig. 4a the hardness in relation to the {0001} fraction is depicted for all TiB_{2+z} coatings deposited. The graph shows a linearly increasing H of >10 GPa (from ≈27 to ≈41 GPa) for <10 % to >99 % {0001} fraction when following the datapoints from the deposition pressure variation p_{out} (green dashed line), which are not influenced by structural/morphological changes. A similar slope in hardness of ≈1 GPa per 10 % {0001} fraction was observed for WB_{2-z} [17] and seems to be therefore, independent of the material system. Interestingly, the highly $21\bar{3}0$ oriented film even exceeds the maximum hardness of ≈41 GPa of the perfectly 0001 oriented films by ≈2 GPa. Hence, this orientation aggravates dislocation movement even more effectively compared to the 0001 orientation, where the pyramidal slip system is preferentially activated [17]. In Fig. 4b, the deposited films exhibiting a {0001} fraction >90 % are highlighted in black square and circular frames (hardness anisotropy effect is excluded), revealing a linearly decreasing trend in hardness of ≈7 GPa (from ≈41 to ≈34 GPa). At this point in the manuscript, it is not yet possible to make a scientifically substantiated statement about this softening effect. Still, it is further elucidated after considering the selected samples' detailed structural and morphological features (see description Figs. 5 and 6).

XRD data has been consulted to evaluate the FWHM of all investigated thin films with a {0001} fraction >90 % to exclude the hardness anisotropy effect. In Fig. 5a the FWHM of the 0002 diffraction peaks are illustrated as a function of increasing B/Ti ratio, revealing a distinct increasing trend from $FWHM_{0002}$ = 0.70°2θ at B/Ti = 2.58 ranging to 1.37°2θ at B/Ti = 4.42. This descending behavior of the coherently diffracting domains (increasing $FWHM_{0002}$) can indicate smaller crystallite sizes of the investigated TiB_{2+z} thin films. The $FWHM_{0001}$ shows a similar trend with increasing B/Ti and is listed in Table A2 in the Appendix A section.

To evaluate the crystallite size of all the TiB_{2+z} thin films with a {0001} fraction >90 % (anisotropy effect is excluded) the Scherrer formula is used (Formula (1)). Fig. 5b highlights the hardness values as a function of decreasing crystallite sizes determined from the 0002 diffraction peaks. A decreasing trend of the film hardness from ≈41 GPa to ≈34 GPa in correlation with decreasing crystallite sizes is depicted in Fig. 5b. In contrast to the Scherrer equation, the Williamson-Hall approach decouples the influence of grain size and micro strains from the peak breadth. Still, it provided inaccurate results (e.g. negative crystallite sizes for some datapoints) when applied for the columnar structured thin films (non-spherical geometries) investigated within this study. However, the Scherrer formula uses the FWHM to evaluate the column sizes, which is also sensitive to structural defects. Here we used the 0002 peak, to guarantee better accuracy concerning peak asymmetry effects.

Consequently, TEM top view observations are conducted exhibiting decreasing column sizes with increasing B content of a $TiB_{2.43}$ and a $TiB_{4.42}$ coating (both with >90 % {0001} fraction), depicted in Fig. 6. The $TiB_{2.43}$ film stoichiometry reveals column sizes of about 10 nm (Fig. 6a and c) declining to <5 nm for the highly super-stoichiometric $TiB_{4.42}$ thin film (Fig. 6b and d). Independent of the films' B content, the TEM observations exhibit 1 to 2 nm thin B-rich tissue phases separating the columns. The tissue phases are indicated as small bright features (representing light elements) in Fig. 6a and b in accordance to [11]. In addition, the STEM observations (Z-contrast) in Fig. 6c and d underline the elemental distribution of light B (dark features) on the column boundaries. SAED analysis exhibited, that B is not forming a separate crystalline phase as only AlB_2 structured TiB_2 is visible (Fig. 6a-i and b-i). Due to the smaller column size of the $TiB_{4.42}$ film (Fig. 6b and

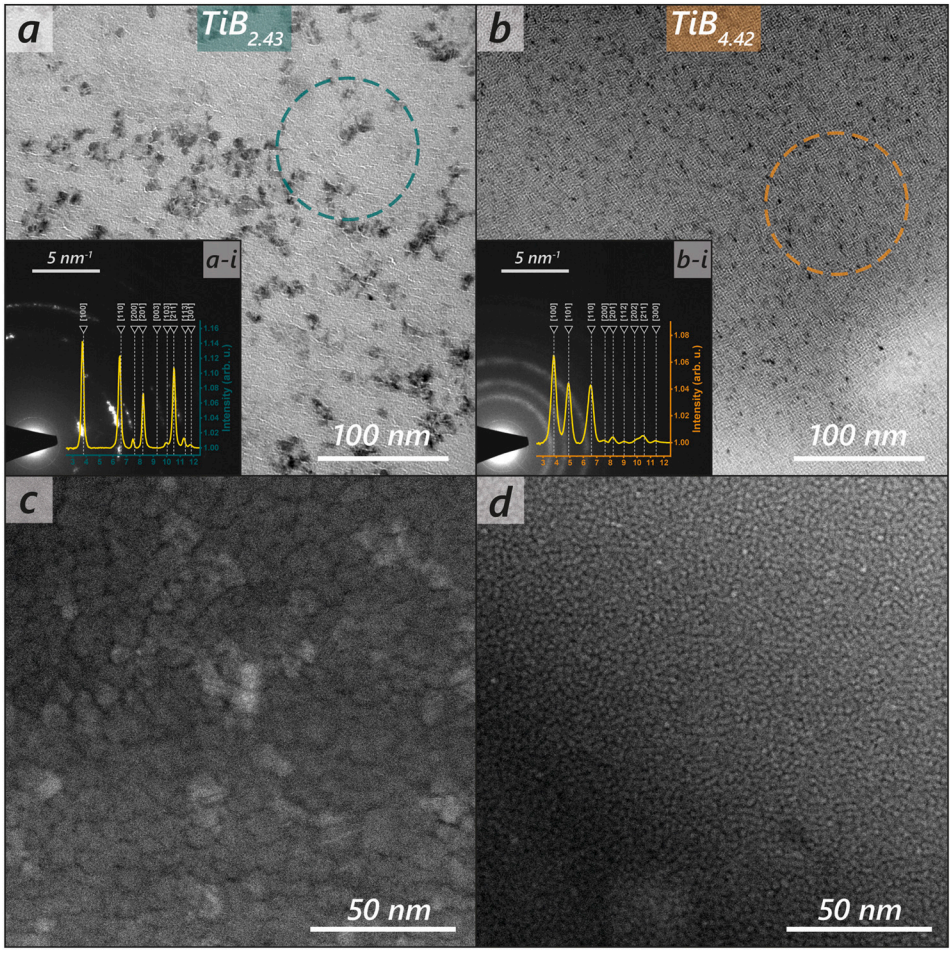

Fig. 6. Bright field TEM top view observations of a $TiB_{2.43}$ (a) and a $TiB_{4.42}$ (b) thin film reveal column sizes in the nanometer range. The dashed circles highlight the areas of the recorded SAED pattern, depicted in a-i and b-i. STEM observations (*Z*-contrast) of the $TiB_{2.43}$ (c) and the $TiB_{4.42}$ (d) exhibit the elemental distribution of light B on the column boundaries.

d) compared to the $TiB_{2.43}$ film (Fig. 6a and c) the surplus B is distributed on the increased column boundary fraction, forming thin B-rich tissue phases.

Thus, the observed drop in hardness when exceeding a B/Ti ratio > 2.4, for all thin films with {0001} fraction >90 %, (see Figs. 4b and 5b) is related to an inverse Hall-Petch effect, describing a softening with decreasing column size, due to preferred column boundary sliding events [7,30,31]. This effect is also conspicuous in Fig. 4a, where H is varying from ≈34 GPa to ≈41 GPa for almost perfectly {0001} oriented films. Residual stresses determined by applying Stoney's equation - using curvature measurements of thin films on silicon substrates - exhibit compressive stresses in the range of −0.5 to −2.5 GPa. Hence, only a minor contribution of the residual stresses on the film hardness is assumed.

The green and orange dashed lines in Fig. 4b indicate samples from decreasing deposition pressure (from 2.0 to 0.4 Pa), revealing an increase in B content and hardness accompanied by an increasing {0001} orientation fraction. Surprisingly, coatings from inner and outer radius exhibit the same trend in increasing {0001} fraction (also depicted in Fig. 3a) and H but at a different B/Ti ratio. This behavior would assume that the hardness of TiB_{2+z} is only minor affected by the B content and/or a B-rich tissue phase (at least in a B/Ti regime of ≈2.0 to ≈3.0), instead mainly by its predominant orientation. The knee in the orange dashed line indicates, when reaching a B/Ti ratio of ≈3.0 (valid for this specific geometrical and compositional conditions) the hardness gets significantly affected by the smaller column size, which would mean that column boundary sliding contributes to a reduction in hardness. Furthermore, it is also conceivable that we would observe a similar trend for our samples from the outer substrate holder position with a pressure variation to even lower process pressures (<0.4 Pa). These findings extend the current knowledge [11] on the predominant hardening mechanisms in super-stoichiometric TiB_{2+z} films.

In addition to the broad approach describing the structure-mechanical behavior of all TiB_{2+z} coatings deposited, four stoichiometries are selected for cantilever bending experiments to analyze the intrinsic fracture toughness. These tests are performed on a $TiB_{2.43}$ (p_{dep} = 1.2 Pa, d_{real} = 124 mm), $TiB_{3.03}$ (p_{dep} = 1.2 Pa, d_{real} = 110 mm), $TiB_{3.19}$ (p_{dep} = 0.4 Pa, d_{real} = 141 mm) and $TiB_{4.42}$ (p_{dep} = 0.4 Pa, d_{real} = 129 mm) coating, with thicknesses between 5 and 6 µm. The slight variation in coating thickness arises from the differences in deposition rate on inner and outer substrate positions. The relation between the fracture toughness, K_{IC}, and B/Ti ratio is summarized in Fig. 7a. The

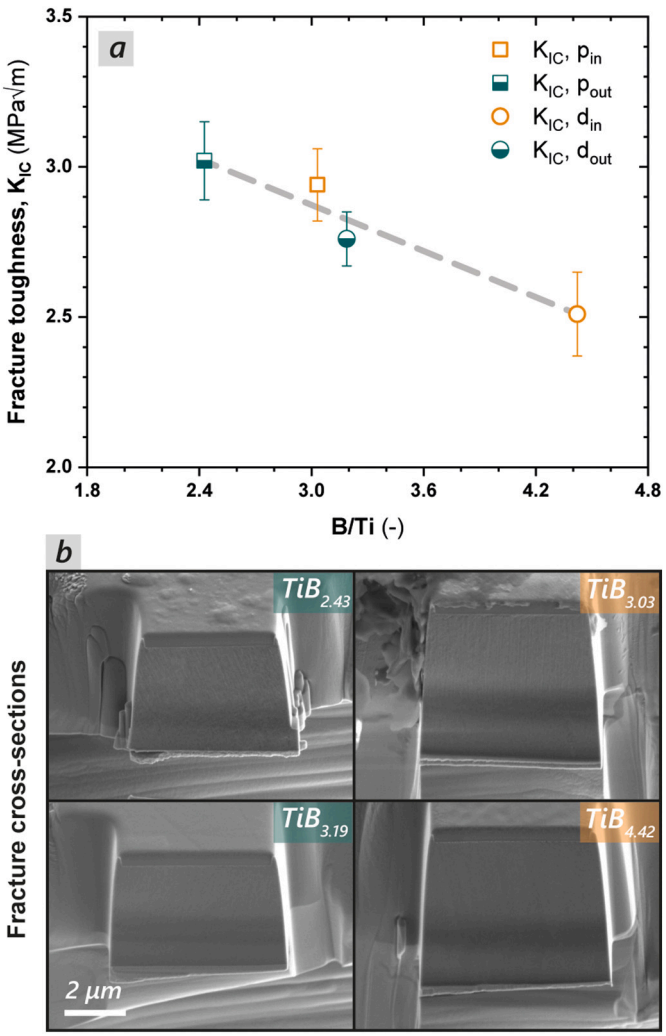

Fig. 7. Intrinsic fracture toughness K_{IC} from micro-cantilever experiments depicted as a function of B/Ti ratio (a). Inner and outer radii placed samples are represented by open orange and half-filled green symbols. Square and circular symbols indicate coatings derived from deposition pressure and distance variation. SEM fracture cross-sections of the tested substrate-free TiB_{2+z} coatings are depicted in b.

plotted intrinsic fracture toughness values have been calculated, after analyzing the fracture cross sections (B, w, a) of the tested films, as depicted in Fig. 7b. The experiments exhibit highest $K_{IC} = 3.02 \pm 0.13$ MPa$\sqrt{m}$ for the lowest B containing $TiB_{2.43}$ coating, linearly decreasing with increasing B/Ti ratio to $K_{IC} = 2.51 \pm 0.14$ MPa$\sqrt{m}$ for $TiB_{4.42}$. In between these outer limits, the K_{IC} slightly decreases to 2.94 ± 0.12 MPa$\sqrt{m}$ for $TiB_{3.03}$ and 2.76 ± 0.09 MPa$\sqrt{m}$ for $TiB_{3.19}$ being only less off the maximum. These results suggest a dependency of K_{IC} on the column size of the TiB_{2+z} films. Here, crack propagation along column boundaries, which in most cases represents the weakest pathways, might be the predominant mechanism. B aggregation on column boundary fractions decreases cohesive column boundary strength, facilitating crack propagation. However, no influence of the crystal orientation on the fracture toughness is observed as all investigated coatings are highly 0001 oriented, being consistent with [17].

4. Conclusion

The structure-mechanical relation of non-reactively DC magnetron sputtered TiB_{2+z} thin films has been thoroughly described in a wide B/Ti range, from almost stoichiometric $TiB_{2.07}$ (B: 67 at. %) up to super-stoichiometric $TiB_{4.42}$ (B: 82 at. %), respectively. Through systematically varying the deposition pressure and distance, we highlight the strong angular distribution of sputtered B and Ti species, whereas B is preferentially emitted along the vicinity of the target normal. A variation in the sputter distance from 64 to 154 mm revealed an even higher impact on the B content (Δ(B/Ti) ≈ 1.24 at $p_{dep} = 0.4$ Pa) compared to the deposition pressure, varied from 0.4 to 2.0 Pa (Δ(B/Ti) ≈ 0.86 at d = 104 mm). This comprehensive variation in deposition conditions revealed a pronounced pressure dependency of the {0001} orientation where lower deposition pressure regimes (up to 1.2 Pa) favor the {0001} orientation. A significant hardness-anisotropy is underlined by the drastic increase of >10 GPa with increasing {0001} fraction, independently on the stoichiometry. Nevertheless, the maximum hardness values (≈41 GPa) are found in the range of B/Ti ≈ 2.4 to 2.8. For increasing B contents (B/Ti ≥ 2.5), the crystallite size of the TiB_{2+z} films decreases (determined with Scherrer's formula)– which leads to a hardness drop of ≈7 GPa. TEM observations underline decreasing column sizes with increasing B content (from ≈10 nm to <5 nm). Hence, the linear drop in H is attributed to preferred column boundary gliding events ascribed to reverse Hall-Petch-like effects for predominantly {0001} oriented thin films (>90 % {0001} fraction). Micro-cantilever bending experiments evinced maximum intrinsic $K_{IC} = 3.02 \pm 0.13$ MPa$\sqrt{m}$ for the $TiB_{2.43}$ coating, slightly decreasing to $K_{IC} = 2.51 \pm 0.14$ MPa$\sqrt{m}$ for $TiB_{4.42}$ owing to decreasing column sizes.

CRediT authorship contribution statement

C. F., R. H., and H. R. conceived the research. C. F. conducted the depositions, structural, and mechanical investigations. A.H. conduced paper reviewing. P. K. performed FIB cantilever preparation, M. W. performed the chemical analysis by ICP-OES supported by A. L. P. P. and O. H. supported the research by providing funding and expertise. H.R. took care about the funding acquisition as well as supervision. All authors then contributed and have given approval to the final version of the manuscript.

Declaration of competing interest

The authors declare that they have no known competing financial interests or personal relationships that could have appeared to influence the work reported in this paper.

Data availability

Data will be made available on request.

Acknowledgements

The financial support by the Austrian Federal Ministry for Digital and Economic Affairs, the National Foundation for Research, Technology and Development and the Christian Doppler Research Association is gratefully acknowledged (Christian Doppler Laboratory “Surface Engineering of high-performance Components”). We also thank for the financial support of Plansee SE, Plansee Composite Materials GmbH, and Oerlikon Balzers, Oerlikon Surface Solutions AG. In addition, we want to thank the X-ray center (XRC) of TU Wien for beam time as well as the electron microscopy center - USTEM TU Wien - for using the SEM and TEM facilities. The authors acknowledge TU Wien Bibliothek for financial support through its Open Access Funding Program. We also want to thank Tomasz Wojcik for his precise TEM investigations.

Appendix A

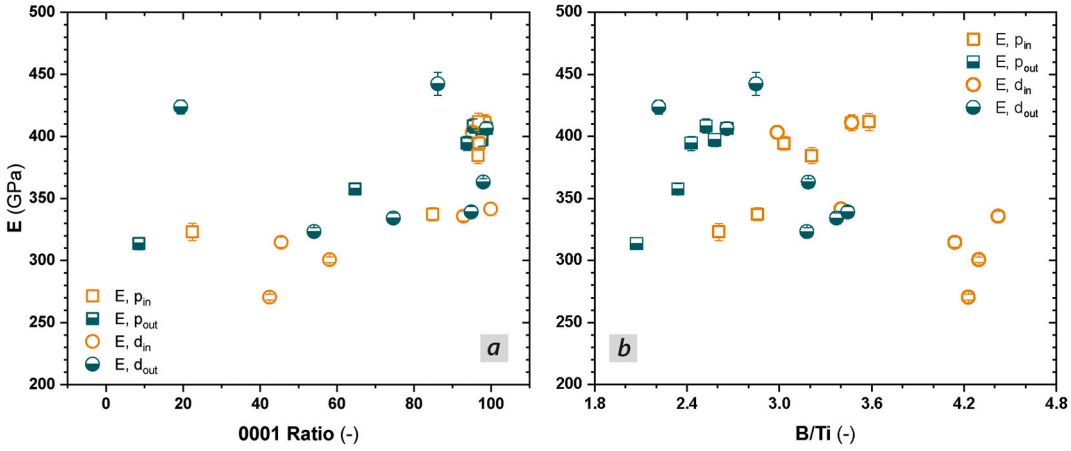

Fig. A1. Young's modulus E as a function of 0001 ratio (a) and B/Ti ratio (b). Open and half-filled data points represent samples from inner and outer substrate positions, respectively. Square and circular symbols indicate coatings from pressure and distance variation, respectively.

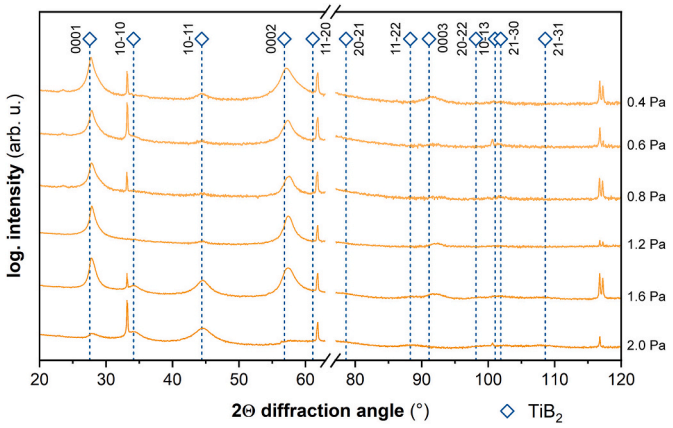

Fig. A2. XRD pattern of all deposited TiB_{2+z} thin films from p_{dep} variation (0.4 to 2.0 Pa) located on the inner radius ($r = 35$ mm) on the circular substrate holder. Peak positions of a characteristic AlB_2 structured TiB_2 (SG191, P6mmm) lattice are marked by dashed blue vertical lines and blue open hexagons. The sharp peaks at 33°, 62° and 117° refer to the silicon substrate.

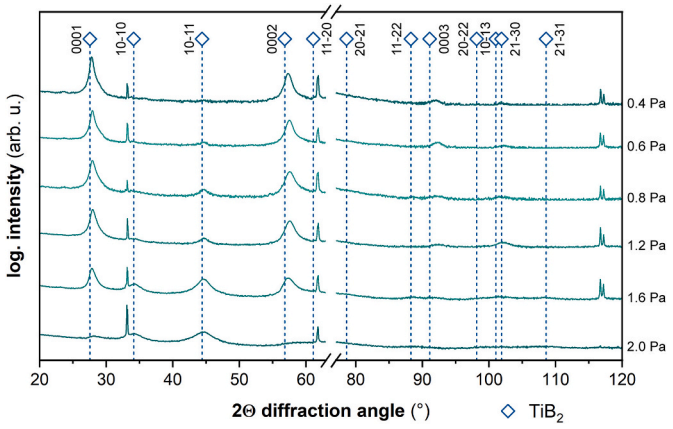

Fig. A3. XRD pattern of all deposited TiB_{2+z} thin films from p_{dep} variation (0.4 to 2.0 Pa) located on the outer radius ($r = 70$ mm) on the circular substrate holder. Peak positions of a characteristic AlB_2 structured TiB_2 (SG191, P6mmm) lattice are marked by dashed blue vertical lines and blue open hexagons. The sharp peaks at 33°, 62° and 117° refer to the silicon substrate.

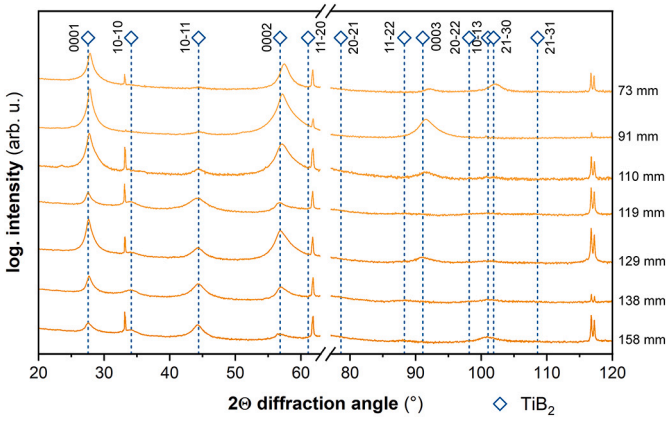

Fig. A4. XRD pattern of all deposited TiB_{2+z} thin films from d_{real} variation (73 to 158 mm) located on the inner radius (r = 35 mm) on the circular substrate holder. Peak positions of a characteristic AlB_2 structured TiB_2 (SG191, P6mmm) lattice are marked by dashed blue vertical lines and blue open hexagons. The sharp peaks at 33°, 62° and 117° refer to the silicon substrate.

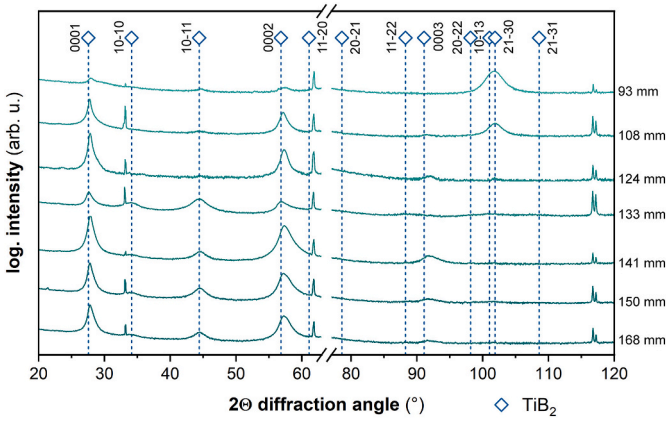

Fig. A5. XRD pattern of all deposited TiB_{2+z} thin films from d_{real} variation (93 to 168 mm) located on the outer radius (r = 70 mm) on the circular substrate holder. Peak positions of a characteristic AlB_2 structured TiB_2 (SG191, P6mmm) lattice are marked by dashed blue vertical lines and blue open hexagons. The sharp peaks at 33°, 62° and 117° refer to the silicon substrate.

The mathematical approaches for calculating the 0001 texture coefficient (TC_{0001}) and {0001} fraction are given by Formulas (A1) and (A2), respectively.

$$TC_{0001} = \frac{\frac{I_{0001}}{I_0^{0001}}}{\frac{1}{6}\cdot\left(\frac{I_{0001}}{I_0^{0001}} + \frac{I_{1000}}{I_0^{1000}} + \frac{I_{10-11}}{I_0^{10-11}} + \frac{I_{0002}}{I_0^{0002}} + \frac{I_{0003}}{I_0^{0003}} + \frac{I_{21-30}}{I_0^{21-30}}\right)} \tag{A1}$$

$$\{0001\}\,fraction = \frac{I_{0001} + I_{0002} + I_{0003}}{I_{0001} + I_{1000} + I_{10-11} + I_{0002} + I_{0003} + I_{21-30}} \tag{A2}$$

Table A1
Reference powder diffraction pattern of hexagonal TiB_2 with space group number 191 and space group P6/mmm (Reference code: 00-035-0741). The listed reference intensities I_0 have been used for calculating TC_{0001}.

hkil	d (Å)	2θ (°)	I_0 (%)
0001	3.229540	27.597	22
$10\bar{1}0$	2.624690	34.132	55
$10\bar{1}1$	2.037030	44.437	100
0002	1.614550	56.991	12
0003	1.076600	91.364	0.5
$21\bar{3}0$	0.991926	101.892	6

Table A2
All deposited TiB_{2+z} coatings are listed by their chemical composition, growth parameter, mechanical properties and structure properties.

Chem. composition			Growth parameter						Mechanical properties				Structure properties					
													FWHM		Scherrer		Orientation	
B/Ti (−)	B (at. %)	Ti (at. %)	p_{dep} (Pa)	d_{real} (mm)	α (°)	loc. (−)	t_{film} (µm)	dep. rate (nm/min)	H (GPa)	SD (GPa)	E (GPa)	SD (GPa)	0001 (°2θ)	0002 (°2θ)	0001 (nm)	0002 (nm)	{0001} fr. (−)	TC_{0001} (−)
2.07	67	33	2.0	124	57	Out	2.11	35	27	1	314	5					0.09	0.62
2.22	69	31	0.4	93	43	Out	2.51	56	42	1	424	6					0.19	0.23
2.34	70	30	1.6	124	57	Out	2.15	36	34	1	358	4					0.65	1.63
2.43	71	29	1.2	124	57	Out	1.96	33	39	1	394	6	0.63	1.09	13.07	8.35	0.93	1.91
2.52	72	28	0.8	124	57	Out	1.72	38	39	1	408	6	0.62	1.05	13.11	8.61	0.95	1.93
2.58	72	28	0.6	124	57	Out	1.54	34	40	1	397	5	0.40	0.70	20.50	12.93	0.98	2.65
2.61	72	28	2.0	110	71	In	2.84	47	28	2	323	7					0.22	1.02
2.66	73	27	0.4	124	57	Out	1.54	34	41	1	406	5	0.39	0.76	21.19	11.91	0.99	2.81
2.85	74	26	0.4	108	51	Out	2.60	43	41	1	442	9					0.86	2.15
2.86	74	26	1.6	110	71	In	2.93	49	33	2	337	5					0.85	1.65
2.99	75	25	0.4	73	61	In	4.47	99	37	1	403	5	0.50	0.95	16.53	9.51	0.95	2.06
3.03	75	25	1.2	110	71	In	2.70	45	38	1	394	5	0.49	0.91	16.83	9.96	0.97	1.89
3.18	76	24	0.4	133	59	Out	2.04	32	32	1	323	3					0.54	1.83
3.19	76	24	0.4	141	61	Out	1.88	31	38	2	363	3	0.47	1.20	17.26	7.55	0.98	1.60
3.21	76	24	0.8	110	71	In	2.35	52	39	1	384	6	0.66	1.11	12.49	8.16	0.97	2.11
3.37	77	23	0.4	150	63	Out	1.63	27	33	1	334	4					0.75	1.44
3.40	77	23	0.4	91	67	In	4.14	69	33	1	342	5	0.27	0.81	30.19	11.23	1.00	1.18
3.44	78	22	0.4	168	66	Out	1.41	24	35	1	339	5	0.59	1.26	13.84	7.21	0.95	2.07
3.47	78	22	0.4	110	71	In	2.38	53	36	1	411	6	0.53	1.35	15.38	6.71	0.98	1.65
3.58	78	22	0.6	110	71	In	2.25	50	36	1	412	7	0.58	1.07	14.01	8.46	0.97	1.83
4.14	81	19	0.4	119	73	In	2.12	42	31	1	315	4					0.46	1.46
4.23	81	19	0.4	158	77	In	1.81	30	29	1	271	2					0.43	1.56
4.30	81	19	0.4	138	75	In	2.15	36	31	1	301	2					0.58	1.94
4.42	82	18	0.4	129	74	In	2.49	41	34	1	336	4	0.50	1.37	16.49	6.60	0.93	1.77

References

[1] J.G. Ryan, S. Roberts, G.J. Slusser, E.D. Adams, The preparation and characterization of titanium boride films, Thin Solid Films 153 (1–3) (1987) 329–339.
[2] H. Blom, T. Larsson, S. Berg, M. Östling, Reactively sputtered titanium boride thin films, J. Vac. Sci. Technol. A Vac. Surf. Film 7 (2) (1989) 162–165.
[3] T. Larsson, H.O. Blom, S. Berg, M. Östling, Reactive sputtering of titanium boride, Thin Solid Films 172 (1) (1989) 133–140.
[4] J. Shappirio, et al., TiB 2 and ZrB 2 diffusion barriers in GaAs ohmic contact technology, J. Vac. Sci. Technol. A Vac. Surf. Film 3 (6) (1985) 2255–2258.
[5] H. Holleck, Material selection for hard coatings, J. Vac. Sci. Technol. A Vac. Surf. Film 4 (6) (1986) 2661–2669.
[6] M. Berger, L. Karlsson, M. Larsson, S. Hogmark, Low stress TiB2 coatings with improved tribological properties, Thin Solid Films 401 (1–2) (2001) 179–186.
[7] N. Kalfagiannis, G. Volonakis, L. Tsetseris, S. Logothetidis, Excess of boron in TiB2 superhard thin films: a combined experimental and ab initio study, J. Phys. D. Appl. Phys. 44 (38) (2011).
[8] X. Cai, et al., Unmasking the anomalous rapid oxidation of refractory TiB2 at low temperatures, J. Eur. Ceram. Soc. 41 (10) (2021) 5100–5108.
[9] J. Thörnberg, et al., Improved oxidation properties from a reduced B content in sputter-deposited TiBx thin films, Surf. Coatings Technol. 420 (May) (2021) 0–5.
[10] T. Glechner, et al., Influence of Si on the oxidation behavior of TM-Si-B2±z coatings (TM = Ti, Cr, Hf, Ta, W), Surf. Coatings Technol. 434 (2022), 128178.
[11] P.H. Mayrhofer, C. Mitterer, J.G. Wen, J.E. Greene, I. Petrov, Self-organized nanocolumnar structure in superhard TiB2 thin films, Appl. Phys. Lett. 86 (13) (Mar. 2005), 131909.
[12] P.H. Mayrhofer, M. Stoiber, Thermal stability of superhard ti-B-N coatings, Surf. Coat. Technol. 201 (13) (2007) 6148–6153.
[13] J. Thörnberg, et al., Microstructure and materials properties of understoichiometric TiBx thin films grown by HiPIMS, Surf. Coatings Technol. 404 (October) (2020).
[14] M.L. Wu, X.W. Lin, V.P. Dravid, Y.W. Chung, M.S. Wong, W.D. Sproul, Conventional and ionized magnetron sputter-deposition of nanocrystalline titanium diboride thin films, Tribol. Lett. 5 (2–3) (1998) 131–134.
[15] C. Schnitter, et al., Effect of low-energy ion assistance on the properties of sputtered ZrB2 films, Vacuum 195 (2022), 110688.
[16] N. Nedfors, O. Tengstrand, J. Lu, P. Eklund, P.O.Å. Persson, U. Jansson, Superhard NbB2 −x thin films deposited by dc magnetron sputtering, Surf. Coat. Technol. 257 (2014) 295–300.
[17] C. Fuger, et al., Anisotropic super-hardness of hexagonal WB2±z thin films, Mater. Res. Lett. 10 (2) (2022) 70–77.
[18] J. Neidhardt, et al., Experiment and simulation of the compositional evolution of Ti-B thin films deposited by sputtering of a compound target, J. Appl. Phys. 104 (6) (2008).
[19] I. Petrov, et al., Controlling the boron-to-titanium ratio in magnetron-sputter-deposited TiB x thin films, J. Vac. Sci. Technol. A Vac. Surf. Film 35 (5) (2017), 050601.
[20] M. Tkadletz, et al., Influence of B content on microstructure, phase composition and mechanical properties of CVD Ti(B, N) coatings, Materialia 21 (2022), 101323.
[21] L. Zauner, et al., Reactive HiPIMS deposition of ti-Al-N: influence of the deposition parameters on the cubic to hexagonal phase transition, Surf. Coat. Technol. 382 (2020), 125007.
[22] M. Weiss, C. Riedl, J. Frank, J. Fleig, A. Limbeck, Quantitative analysis of the platinum surface decoration on lanthanum strontium iron oxide thin films via online-LASIL-ICP-MS, Microchem. J. 166 (2021), 106236.
[23] E.J. Sonneveld, J.W. Visser, Automatic collection of powder data from photographs, J. Appl. Crystallogr. 8 (1) (1975) 1–7.
[24] W.C. Oliver, G.M. Pharr, An improved technique for determining hardness and elastic modulus using load and displacement sensing indentation experiments, J. Mater. Res. 7 (6) (1992) 1564–1583.
[25] K. Matoy, et al., A comparative micro-cantilever study of the mechanical behavior of silicon based passivation films, Thin Solid Films 518 (1) (2009) 247–256.
[26] "https://www.originlab.com/doc/Origin-Help/Fitted_Curve_Plot_Analysis.".
[27] Natl. Bur. Stand. (U. S.) Monogr. 25 1985, 21, 125.
[28] D. Walton, The orientation of vapour deposits, Philos. Mag. A J. Theor. Exp. Appl. Phys. 7 (82) (1962) 1671–1679.
[29] Y. Zhang, S. Sanvito, First-principles investigation of the thermodynamic stability of MB2 materials surfaces (M = Ti/Zr/Hf), J. Am. Ceram. Soc. 101 (9) (2018) 4118–4127.
[30] J. Schiøtz, F.D. Di Tolla, K.W. Jacobsen, Softening of nanocrystalline metals at very small grain sizes, Nature 391 (6667) (1998) 561–563.
[31] S. Zhang, D. Sun, Y. Fu, H. Du, Recent advances of superhard nanocomposite coatings: a review, Surf. Coat. Technol. 167 (2–3) (2003) 113–119.